Hindawi
Geofluids
Volume 2021, Article ID 9432323, 13 pages
https://doi.org/10.1155/2021/9432323

Research Article

Study on Air Void Characteristics and Hydraulic Characteristics of Porous Asphalt Concrete Based on Image Processing Technology

Zhanqi Wang[1], **Jianguang Xie**[1], **Lei Gao**[1], **Yanping Liu**[1] and **Kuan Li**[1,2]

[1]*Department of Civil and Airport Engineering, Nanjing University of Aeronautics and Astronautics, Nanjing 211106, China*
[2]*Jiangsu Sinoroad Engineering Technology Research Institute Co. Ltd., Nanjing 211806, China*

Correspondence should be addressed to Jianguang Xie; xiejg@nuaa.edu.cn and Lei Gao; glzjy@nuaa.edu.cn

Received 24 August 2021; Accepted 14 September 2021; Published 14 October 2021

Academic Editor: Yu Wang

The appearance of porous asphalt (PA) pavement is to solve the problem of road ponding in rainy days. The internal air voids in PA pavement are the main functional structure that determines its drainage performance. It is of great practical significance to find out the relationship between void drainage capacity and air voids. This paper is aimed at researching the relationship between three-dimensional (3D) pore structures and drainage performance of PA concrete. Four samples were formed and scanned by CT equipment to obtain the internal cross-sectional CT images. Image dodging algorithm and OTSU method were conducted to deal with these CT images for segmenting them into three subimages (void image, asphalt mortar image, and aggregate image) according to the three components of PA concrete. The voids on void images were identified and classified into three groups according to the three kind of pores (interconnected pore, semi-interconnected pore, and closed pore) and reshaped them into 3D pore structures according to the overlapping principle. Then, the volume and size distribution of the pores was analyzed. Besides, this research mainly focused on the influence of several parameters obtained from interconnected pores on the drainage performance of PA concrete at last. The permeability coefficient of PA concrete samples was tested, and equations between permeability coefficient and void content were fitted linearly. The distribution of hydraulic radius and cross-sectional area ratio was calculated and researched by statistical methods. A new parameter, perimeter variation coefficient, is proposed to study the influence of boundary wall roughness on the drainage performance. At last, equivalent drainage channel was drawn to reflect the drainage capacity of PA concrete.

1. Introduction

In the engineering field, water stability and drainage problems have always been perplexing engineers and scholars [1–4]. Porous asphalt (PA) pavement is known as a kind of environmental friendly pavement due to its drainage, noise reduction, and antiskid properties [5–7]. PA pavement was originally designed for rapidly draining the rainwater to improve driving safety on rainy days. The drainage performance is closely linked with its interconnected pore structures [8, 9]. However, pore structures usually exist in PA concrete in extremely complex geometry, which poses a great challenge to study the relationship between drainage performance and characteristic parameters of pore structures.

Void parameters (such as void content and size) are commonly used indicators instead of characteristic parameters of pore structures for researching its influence on drainage performance or other properties by most researchers [10–14]. Void parameters are usually obtained from two-dimensional cross-sectional images by using computed tomography (CT) technology combined with image processing technology. Although it is relatively easy to obtain void parameters, more efforts are needed to develop and propose pore characteristic parameters of pore structures, so as to study its influence on drainage performance more accurately. Three-dimensional (3D) reconstruction of pore structures is an important step to research its influence on drainage performance or other properties. Due to the

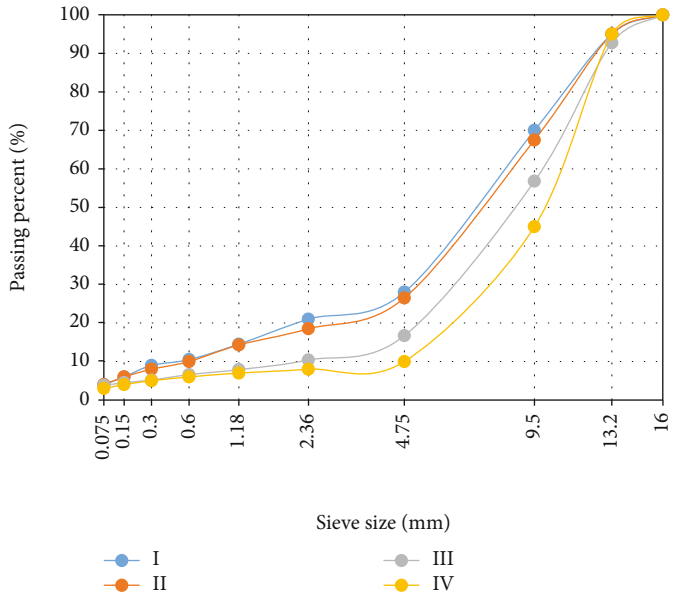

Figure 1: Aggregate gradation.

complexity of pore geometry, there is still a lack of effective methods to reconstruct the 3D geometry and obtain characteristic parameters of pore structures at present, and only a few researchers have done some work in this field [15–17]. Gruber et al. [15] reconstructed the 3D model of pores and simulated the fluid flow in PA concrete sample by Avizo and ANSYS 12.0. Zhao et al. [16] proposed a method to separate the valid and invalid interconnected pores in PA concrete. Besides, in terms of drainage performance, most researches generally regarded PA concrete as permeable medium to study its macro drainage performance, but not to study the impact of its structure properties on drainage performance from the micro structure perspective [18–20]. Garcia et al. [18] analyzed the permeability reduction in drainage asphalt mixtures through a self-developed device and using the coefficient of permeability as the indicator to reflect the drainage performance of drainage asphalt mixtures. Aboufoul et al. [19] investigated the effects of air void topology on hydraulic conductivity in asphalt mixtures by using 3D printing technology, and permeability coefficient was also used for predicting the hydraulic conductivity.

In this paper, the authors tried to find the key parameters affecting hydraulic characteristics based on image processing technology, which paves the way for further revealing the drainage characteristics of PA concrete. First, 3D pore structures were successfully reconstructed by overlapping principle. Second, the volume and size distribution of pores was analyzed. Third, the permeability coefficient of PA concrete samples was tested and equations between permeability coefficient and void content were fitted linearly. At last, several key hydraulic parameters affecting hydraulic characteristics were studied.

2. Materials and Mix Design

Four PA concrete (PAC-13) specimens were taken as the research object in this paper whose target void content was set to be 16%, 18%, 20%, and 22%, respectively. Due to mold size, the specimens were formed with the same size of 300 mm × 300 mm × 40 mm, in which the coarse aggregate was basalt, the fine aggregate was basalt machine-made sand, and appropriate amount of limestone powder was used as mineral powder filler. In addition, SBS-modified asphalt mixed high-viscosity additives (HVA) were used as binder to increase the adhesion between asphalt mortar and aggregates. The aggregate gradation is shown in Figure 1.

3. CT Image Processing

CT scanning technology was used to scan the specimens to observe the internal structure, mainly observing the pore structures in PA concrete. Due to the allowed sample size of CT equipment, the four specimens were, respectively, cut into nine pieces with the same size of 100 mm × 100 mm × 40 mm, and the central piece was taken as target sample I~IV to be scanned. Besides, the samples were scanned along the thickness direction with an interval of 0.14 mm. In the process, 275, 272, 270, and 273 CT images were generated from the sample I~IV, respectively.

Image processing is an important step to obtain and evaluate the characteristic of pore structures. A reliable image segmentation algorithm is indispensable and essential to segment these CT images. Image processing generally involves four steps: image graying (RGB to gray), median filtering, contrast enhancement, and image segmentation [6, 16]. Image segmentation is the most important step in the whole process; the segmentation algorithm directly determines the accuracy of subimages after segmentation. As we know, the OTSU algorithm [21] is a commonly used method to segment gray images due to its advantages such as simplicity, efficiency, and accuracy. The OTSU algorithm describes a method to separate target object and background in a digital image by finding out the key thresholds for

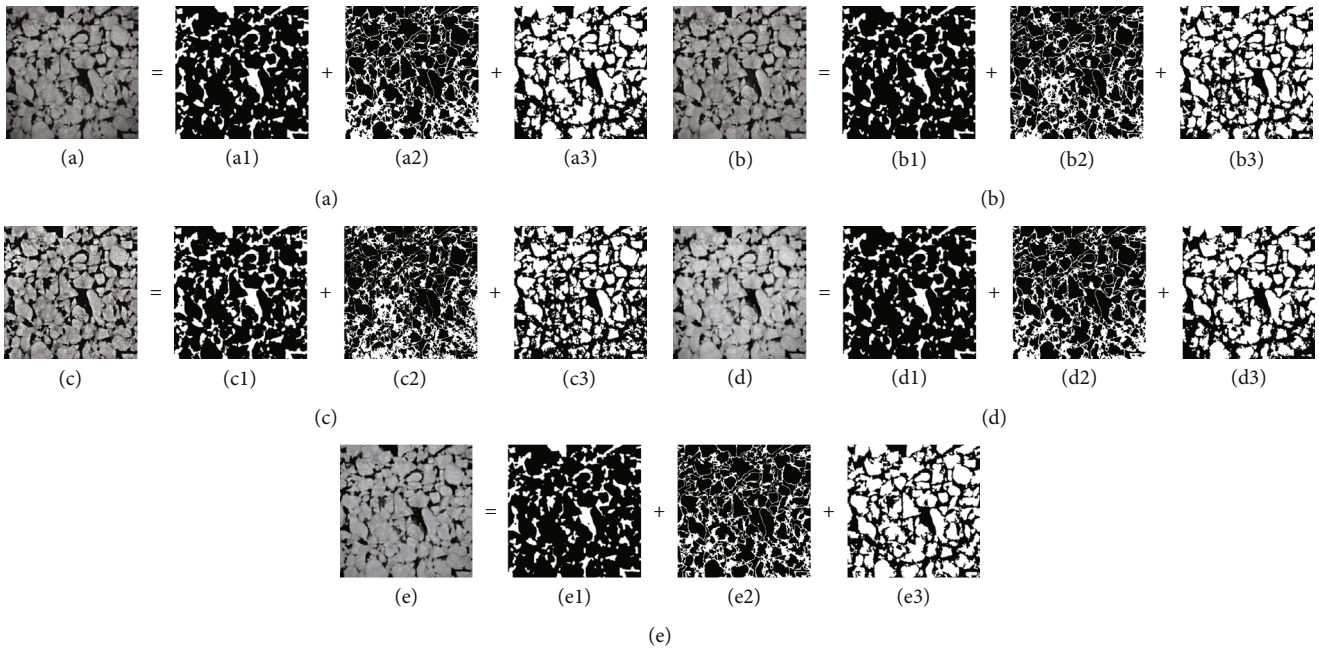

Figure 2: CT image segmentation: (a) without dodging; (b) MASK dodging; (c) Retinex dodging; (d) homomorphic filter dodging; (e) 2D gamma dodging; (*1) void; (*2) asphalt mortar; (*3) aggregate. The range of "$*$" is (a)–(e).

classifying all the pixels into different groups. In this paper, the OTSU algorithm was also used in image segmentation. All the CT images were separated into three subimages by the OTSU algorithm according to the three components (void, asphalt mortar, and aggregate) of PA concrete, as shown in Figure 2. However, the quality of subimages was always disappointing while CT images without further improved process. For example, Figures 2(a1), 2(a2), and 2(a3) are subimages of CT image Figure 2(a), whose white areas stand for void, asphalt mortar, and aggregate, respectively. It is obvious in the figures that a part of aggregate was missing and wrongly classified as asphalt mortar or void. In most cases, CT images need to be preprocessed by specific methods before segmentation to eliminate some specific defects that affect the accuracy of segmentation. In this research, a universal phenomenon was found in most CT images that the aggregate in the center shows brighter (with larger intensity) while the aggregate at four corners shows darker (with smaller intensity), as shown in Figure 2(a). So it can be inferred that the uneven illumination may be the main defect that affects the accuracy of segmentation which needs to be preprocessed. Subsequently, a series of image dodging algorithms were conducted to unify the illuminance component of CT images before segmentation.

To meet different image processing demands in different fields, a variety of image dodging algorithms have been developed by researchers, such as MASK dodging [22], homomorphic filter dodging [23], Retinex dodging [24], and 2D gamma dodging [25]. In this paper, they were all conducted on the CT images to unify the illuminance component and then separated into three subimages, respectively, as shown in Figure 2. It is easy to find that CT image preprocessed by 2D gamma dodging shows the best segmentation effect: less aggregate missing and asphalt mortar and void being closest to actual situation. It should be noted, however, that this research mainly focused on the pore structures in PA concrete. A novel method to identify and reconstruct pore structures was introduced in Section 4, and the proportion of pore structures that connected with the outside space was calculated by MATLAB. The results are shown in Table 1.

Table 1: Proportion of pore structures that connected with the outside space (%).

Sample		I	II	III	IV
Without dodging	V_c	13.10	14.88	21.67	25.12
	E	34.89	7.15	7.30	3.26
2D gamma	V_c	12.93	14.42	21.03	24.47
	E	33.18	3.85	4.12	5.77
MASK	V_c	13.05	15.11	22.27	25.89
	E	34.44	8.80	10.23	0.27
Retinex	V_c	18.25	21.53	29.13	30.21
	E	87.99	55.04	44.21	16.33
Homomorphic	V_c	13.28	15.08	21.91	25.35
	E	36.82	8.60	8.47	2.37
V_p		9.71	13.89	20.20	25.97

Furthermore, the four samples were placed into a measuring cup with proper amount of distilled water to measure the proportion of pore structures that connected with the outside space according to Equation (1). The measuring cup is shown in Figure 3, and measuring results are listed in Table 1. In addition, the errors between measured values

(a) (b)

Figure 3: Measuring device.

and calculated values were obtained by Equation (2) and also listed in Table 1.

$$V_p = \frac{(V_a - V_W)}{V_s}, \tag{1}$$

$$E = \frac{|(V_p - V_c)|}{V_p}, \tag{2}$$

where V_p is the measured proportion of pore structures that connected with the outside space, V_a is the volume of distilled water, V_w is the volume of distilled water with sample, V_s is the volume of sample, V_c is the calculated proportion of pore structures that connected with the outside space, and E is the error between V_p and V_c.

From Table 1, it can be concluded that image dodging could improve the visual and sensory effects, but limited help for image segmentation. Compared with the measured values and errors, values calculated from the CT images that are preprocessed by 2D gamma image dodging are more accurate and reliable than the others. Values calculated from images preprocessed by Retinex image dodging show the maximum error. Considering the image segmentation effect and calculation accuracy, 2D gamma dodging algorithm was chosen to unify illumination of CT images for further research, eventually.

4. Identification and Reconstruction of Pore Structures

4.1. Identification of Pore Structures. As mentioned above, a series of CT images was obtained and separated into three subimages, including void image, asphalt mortar image, and aggregate image. Pore structures in PA concrete could be reconstructed through an appropriate algorithm by using air voids in void images. Actually, such an algorithm is available: overlapping principle. It is easy to imagine that air voids in two adjacent void images that share a common overlapping area, from the top view, must belong to the same pore structure if the interval of the two void images is close enough along the thickness direction. According to the overlapping principle, all the air voids in different CT images can be identified and classified into independent groups that belong to different pore structures. Thus, all the air void groups can be reshaped into pore structures by MATLAB, respectively.

4.2. Reconstruction of Pore Structures. Pore structures in PA concrete mainly can be classified into three types: interconnected pore (IP), semi-interconnected pore (SP), and closed pore (CP). Interconnected pore refers to the pore with two open ends that connected with the outside space at the top and bottom of samples. Semi-interconnected pore refers to the pore with an open end and a dead end. Closed pore refers to the pore with two dead ends that isolated from the outside space. According to the overlapping principle, a MATLAB program was properly edited and executed to reconstruct all the pore structures. Figure 4 shows all the interconnected pore structures in the four samples. It can be seen that samples I~IV contain 3, 3, 1, and 1 interconnected pore, respectively. Pore structures in image (a)~(c) were reconstructed from sample I, images (d)~(f) were reconstructed from sample II, images (g) and (h) were reconstructed from samples III and IV, respectively. However, it is discouraged that all the pores have a complex and disorderly structure which turned out to be a challenge for further research. Besides, the samples also contain thousands of closed pores and dozens of semi-interconnected pores, which are not listed in Figure 4 due to the space limitation of the paper. In addition, it also can be inferred that the sample formed by the aggregate gradation with smaller target void content is more likely to form multiple independent interconnected pores, while the sample formed by the aggregate gradation with larger target void content is more likely to form single overall interconnected pore.

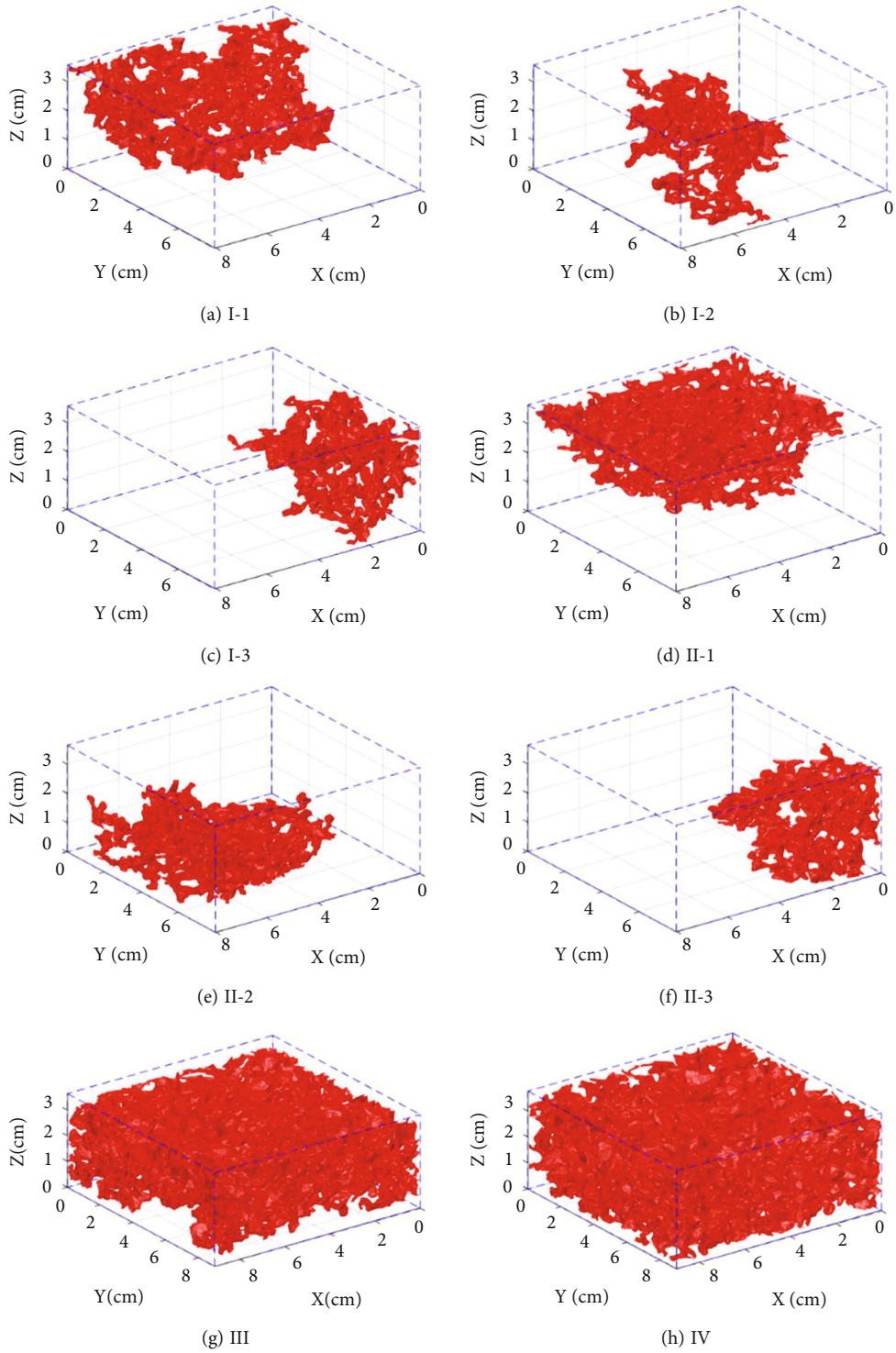

Figure 4: Interconnected pore structures.

5. Distribution of Pore Structures

5.1. Volume Distribution. There are generally thousands of pore structures in PA concrete, most of which are micro closed pores. The number and volume of pore structures in the four samples were calculated and listed in Table 2 after 3D reconstruction process. It can be seen that the number of closed pores with volume less than 1 mm^3 accounts for more than 70% of the total number; however, their cumulative volume accounts for a very small proportion of the total volume of all the pores in the samples, which is less than 0.5%. In specimens I-V, the cumulative volume of all closed pores accounts for 8.53%, 7.62%, 1.97%, and 0.28% of the total pore volume, respectively. And the cumulative volume

Table 2: Number and volume distribution of pore structures.

Volume range (mm^3)		I		II		III		IV	
		Num.	Vol.	Num.	Vol.	Num.	Vol.	Num.	Vol.
0~1	IP	0	0.00	0	0.00	0	0.00	0	0.00
	SP	31	9.94	29	9.51	38	7.96	38	8.56
	CP	945	158.94	1101	193.64	1378	120.29	378	38.53
1~10	IP	0	0.00	0	0.00	0	0.00	0	0.00
	SP	19	76.93	21	64.22	5	19.03	6	11.13
	CP	212	675.86	263	838.51	111	358.68	42	136.78
10~100	IP	0	0.00	0	0.00	0	0.00	0	0.00
	SP	6	179.23	8	377.49	3	70.19	2	21.75
	CP	68	2060.12	68	2182.76	28	574.10	5	69.49
100~500	IP	0	0.00	0	0.00	0	0.00	0	0.00
	SP	5	927.52	2	374.09	0	0.00	0	0.00
	CP	7	1141.29	5	782.71	3	401.34	0	0.00
>500	IP	1	41566.90	1	47654.50	1	72185.50	1	87136.70
	SP	1	530.80	0	0.00	0	0.00	0	0.00
	CP	0	0.00	0	0.00	0	0.00	0	0.00
Total		1295	47327.53	1498	52477.43	1567	73737.09	472	87422.94

of all semi-interconnected pores accounts for 3.64%, 1.57%, 0.13%, and 0.05% of the total pore volume, respectively. The volume of interconnected pore is the absolutely dominant part of the total pore volume in samples I~IV, accounting for 87.83%, 90.81%, 97.90%, and 99.67%, respectively. It should be noted that each sample contains only one interconnected pore in the table. Actually, PA concrete with lower void content may contain several independent interconnected pores. It was found that the surface texture of samples has an important influence on 3D reconstruction process. The surface texture is an open boundary with a certain depth. All the independent interconnected pores will intersect with the surface texture at the top or bottom to form a whole. Therefore, the CT image within the texture depth must be deducted in the 3D reconstruction process to achieve the purpose of separating independent interconnected pores. For instance, three independent interconnected pores are separated from samples I and II when deducting CT images covering the texture depth in the 3D reconstruction process.

5.2. Size Distribution. As we know, the size of pore structures is definitely a significant factor that directly determines the drainage performance of PA concrete. However, due to the complex geometry of pore structures, it is difficult to find a reasonable parameter to characterize its size. In this research, equivalent diameter of voids on each CT images was calculated to reflect the size of pore structures from the perspective of statistics, as shown in Figure 5. Equivalent diameter refers to the diameter of a circle whose area equal to the void. It can be seen that the void size is mainly distributed below 2.61 mm, most of which belongs to interconnected pores. The size of voids belonging to closed pores and semi-interconnected pores is mainly distributed below 5.21 mm. In terms of interconnected pores, void size is mainly below 5.21, but the distribution range is relatively wide, and the maximum value is greater than 20.86 mm. With the increase of void content, the proportion of void with large size gradually increases.

6. Hydraulic Characteristics

PA pavement is aimed at quickly removing the rain water, increasing the skid resistance of pavement to improve the driving safety when it was born in the world. Pore structures act as a drainage pipe to drain rain water from pavement surface. The drainage performance of PA pavement depends on the size and geometry of pores. Due to the complex geometry of pores, it is hard to find a representative parameter to evaluate its drainage performance. Some researchers [18, 19] considered PA concrete sample as a whole to test its permeability coefficient for evaluating its drainage performance according to Darcy's law [26] (Equation (3)) which was first proposed and used to test the permeability of soils. Although permeability coefficient may be a good choice for evaluating drainage performance in a sense, it is still a challenge to reveal the internal relationship between drainage performance and geometry of pores.

$$Q = kA\frac{\Delta H}{L}, \tag{3}$$

where Q is the seepage water volume per unit time, cm^3/s; k is the permeability coefficient, cm/s; A is the top surface area of sample to be tested, cm^2; ΔH is the water head difference between top and bottom of sample to be tested, cm; and L is the thickness of sample to be tested, cm.

6.1. Permeability Coefficient. According to Darcy's law, permeability coefficient of samples I-IV was tested by constant

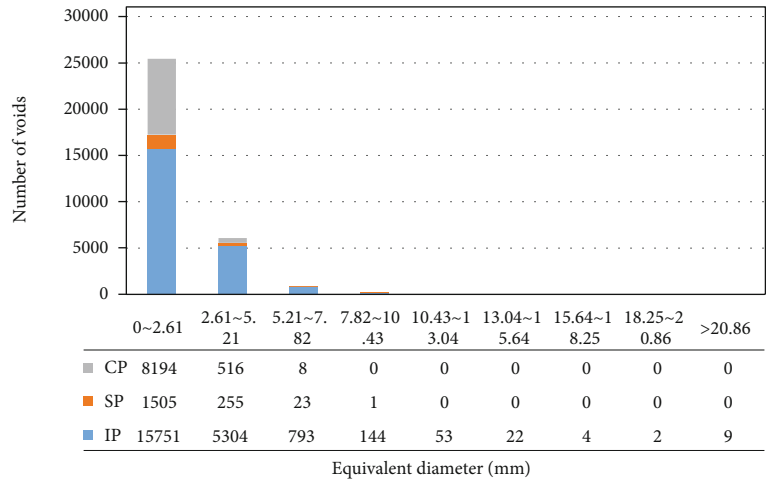

(a) I

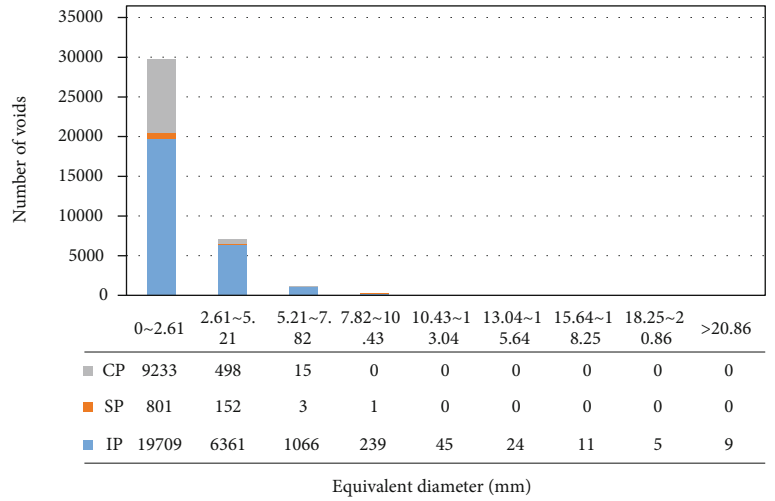

(b) II

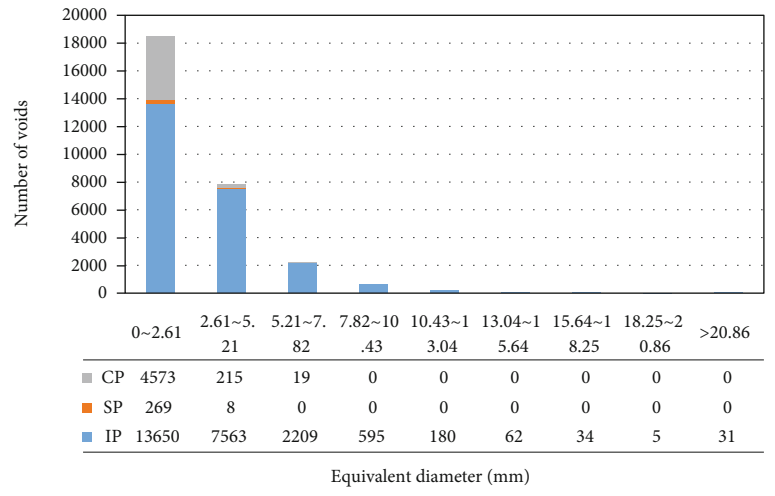

(c) III

Figure 5: Continued.

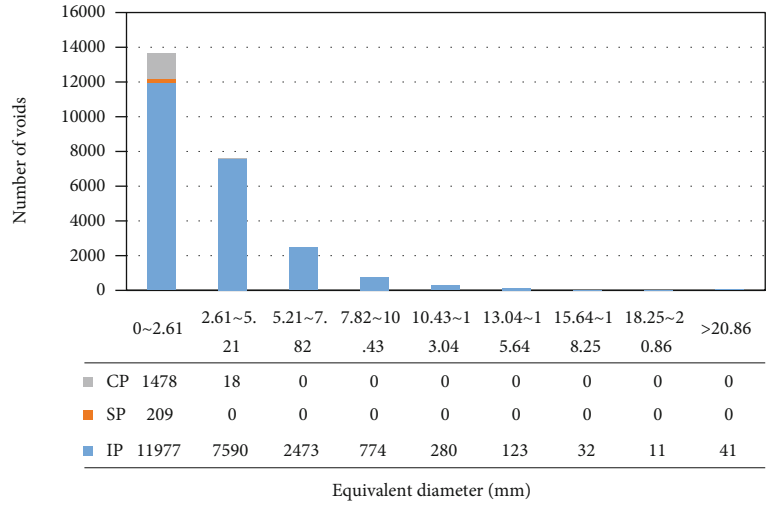

(d) IV

Figure 5: Size distribution of voids.

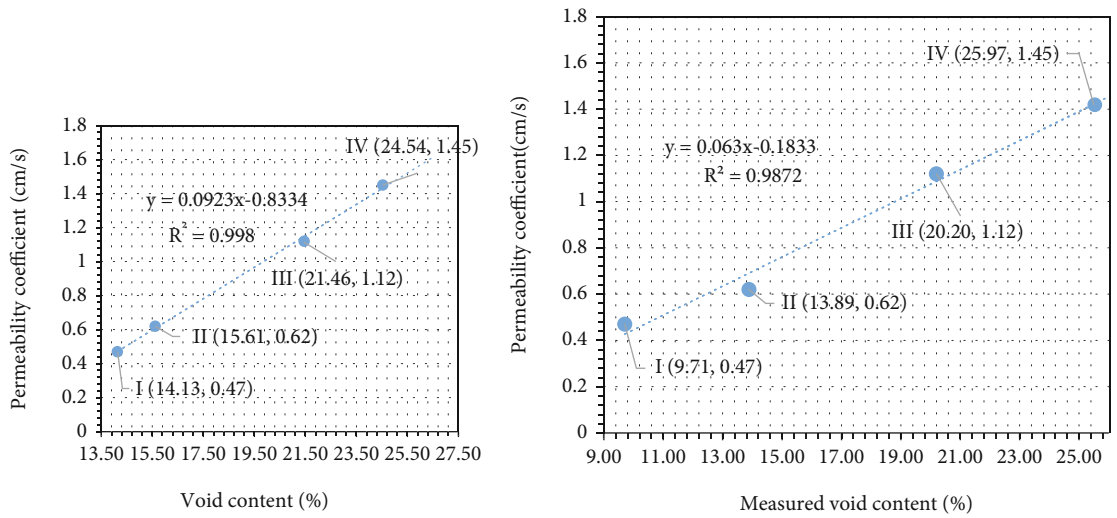

(a) (b)

Figure 6: Relationship between permeability coefficient and void content.

water head method [26] in this research and the results are shown in Figure 6. Figure 6(a) shows the relationship between permeability coefficient and void content which was calculated from CT images. It can be seen that there is a highly linear positive correlation between permeability coefficient and void content. The correlation coefficient reaches 0.998. Figure 6(b) shows the relationship between permeability coefficient and measured void content V_p. It should be noticed that measured void content only involves the proportion of pore structures that connected with the outside space. Likewise, it can be found that the permeability coefficient also shows a high linear correlation with the measured void content, and the correlation coefficient reaches 0.987.

6.2. Hydraulic Parameters. In Equation (3), ΔH refers to the mean value of water head loss, and L refers to the sample thickness rather than the seepage path. Actually, the flow pattern of water in the pore structures is extremely complex; due to the complex geometry of pores, it is hard to find an effective method for revealing the relationship between water head loss and flow pattern of water. This research mainly focused on some key parameters and analyzed their variation law, which lays a foundation for further study of hydraulic characteristics.

As a kind of Newtonian fluid, flow resistance will be produced in the process of water flow due to its viscosity. To overcome the resistance, a part of mechanical energy will be consumed, resulting in head loss. There are two main reasons for the water head loss. One is the influence of viscosity. The interaction between water and solid wall boundary causes uneven velocity distribution on the cross section, which leads to friction resistance in the water flow. The liquid needs to consume a part of energy to overcome the friction resistance. The other is the influence of solid wall boundary. The sharp change of boundary shape will change

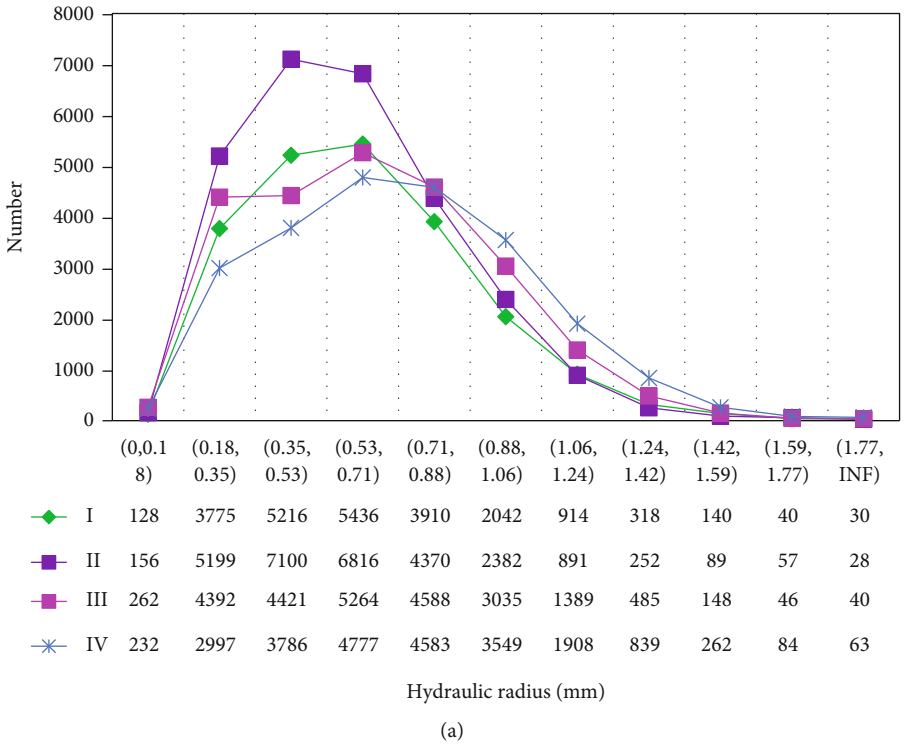

(a)

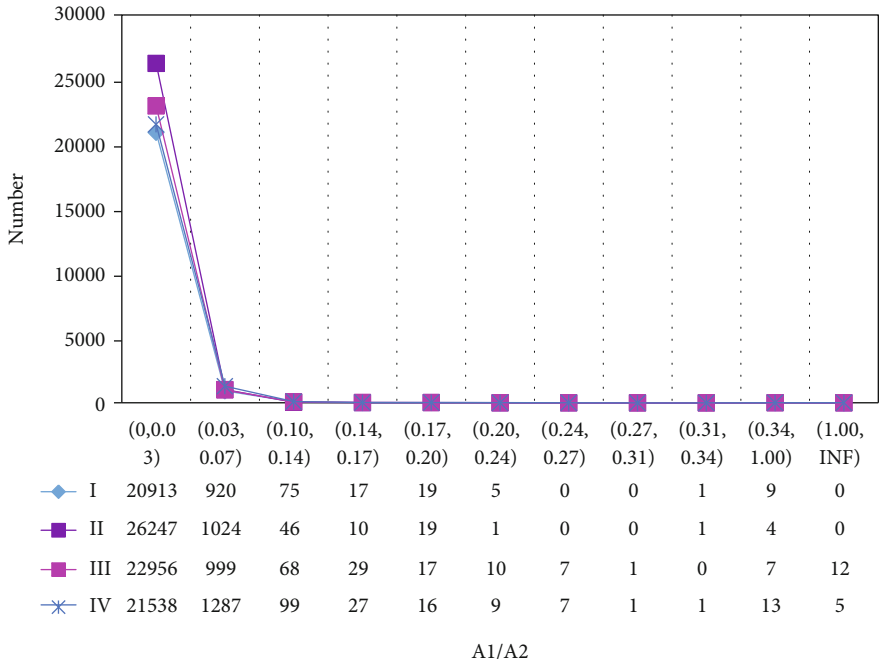

(b)

Figure 7: Distribution of hydraulic radius and A_1/A_2.

the internal structure of water flow and produce vortex flow. The particles in the flow will collide with each other to convert kinetic energy and potential energy. In this process, a part of mechanical energy is converted into heat energy, resulting in energy loss. Besides, the head loss is also related to the microscopic motion of the liquid. Due to the microscopic motion, flow patterns of water can be divided into two types: laminar flow and turbulent flow. Osborne Reynolds [27, 28] has revealed the different nature of the two flow patterns through experiments in the 1880s and studied the relationship between head loss and pipe diameter, wall roughness, and velocity. According to the different reasons causing the water head loss, it can be generally divided into two parts, namely, the water head loss along

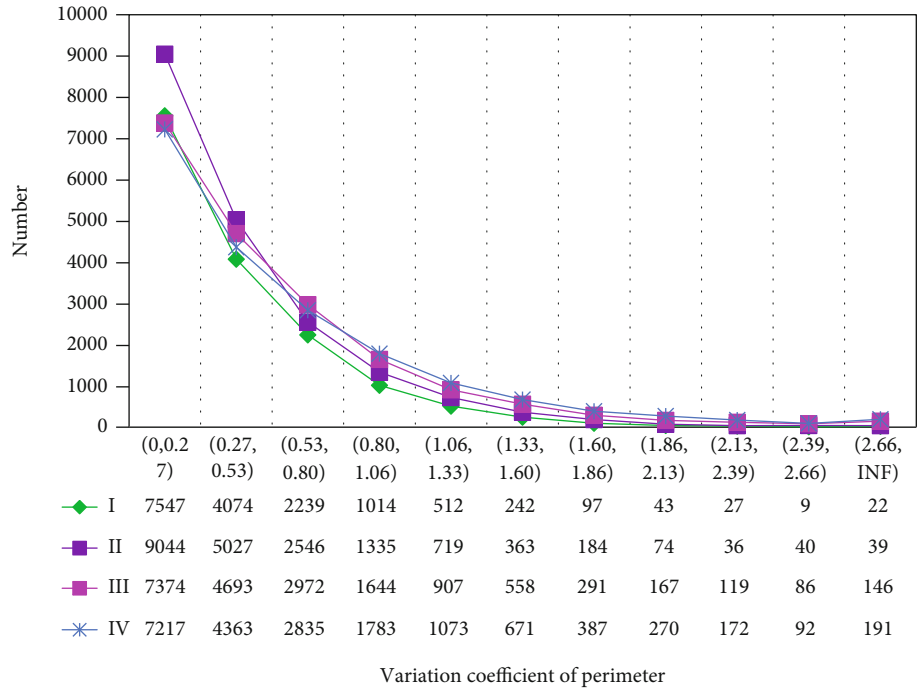

Figure 8: Distribution of perimeter variation coefficient.

flow path and the local water head loss. The general calculation equations are as follows [27]:

$$h_f = \lambda \frac{l}{4R} \frac{v^2}{2g}, \tag{4}$$

$$\lambda = f\left(R_e, \frac{\Delta}{R}\right), \tag{5}$$

$$h_j = \zeta \frac{v^2}{2g}, \tag{6}$$

$$\zeta = f\left(\frac{A_1}{A_2}\right), \tag{7}$$

where h_f is the water head loss along flow path, λ is the resistance coefficient along flow path, l is the flow path, R is the hydraulic radius, Δ is the boundary wall roughness, R_e is the Reynolds number, v is the flow velocity, g is the acceleration of gravity, h_j is the local water head loss, ζ is the local resistance coefficient, and A_1/A_2 is the cross-sectional area ratio at cross section change.

In Equations (4)–(7), there are many unknown parameters that need to be determined. Only R and A_1/A_2 can be directly calculated from the CT images while the others are hard to obtain. Figure 7 shows the distribution of R and A_1/A_2 of interconnected pores in samples I~IV. Hydraulic radius is an important parameter that can comprehensively reflect the influence of cross-sectional shape and size on average velocity. A_1/A_2 can reflect the size change on each cross section of pores. It can be concluded from Figure 7(a) that hydraulic radius is mainly distributed in the range of [0.18, 0.88) mm, accounting for 83.54%, 85.90%, 77.54%, and 69.94% of the total number, respectively, in samples I~V, and the curves gradually flatten with the increase of specimen number, indicating that with the increase of void content, the number of larger voids increases gradually, and the drainage capacity increases in a sense. Besides, it can be seen from Figure 7(b) that the area ratio of adjacent cross sections of interconnected pores is mainly below 0.1, accounting for 99.43%, 99.71%, 99.38%, and 99.24% of the total number, respectively, in samples I~IV, indicating that the geometry of pore structures in PA concrete is extremely complex, which poses a very difficult challenge to the study of its drainage performance or other performances. Meanwhile, it can be found that almost all the values of A_1/A_2 are less than 1, indicating that the size of voids near the top is larger than that near the bottom.

In Equation (5), λ is the function of R_e, R, and Δ. Δ, called boundary wall roughness, refers to the average value of bulge height of boundary wall, which is an important factor that cannot be ignored. For pipe with regular shape, the roughness can be easily obtained, but for the pore structure in porous asphalt concrete, it is almost impossible to define and obtain the boundary wall roughness due to its complex shape. In this research, another similar parameter, called perimeter variation coefficient, was defined to reflect the boundary wall roughness. The perimeter variation coefficient is defined as follows:

$$C_R = \frac{P_o - P_c}{P_c}, \tag{8}$$

where C_R is the perimeter variation coefficient, P_o is the

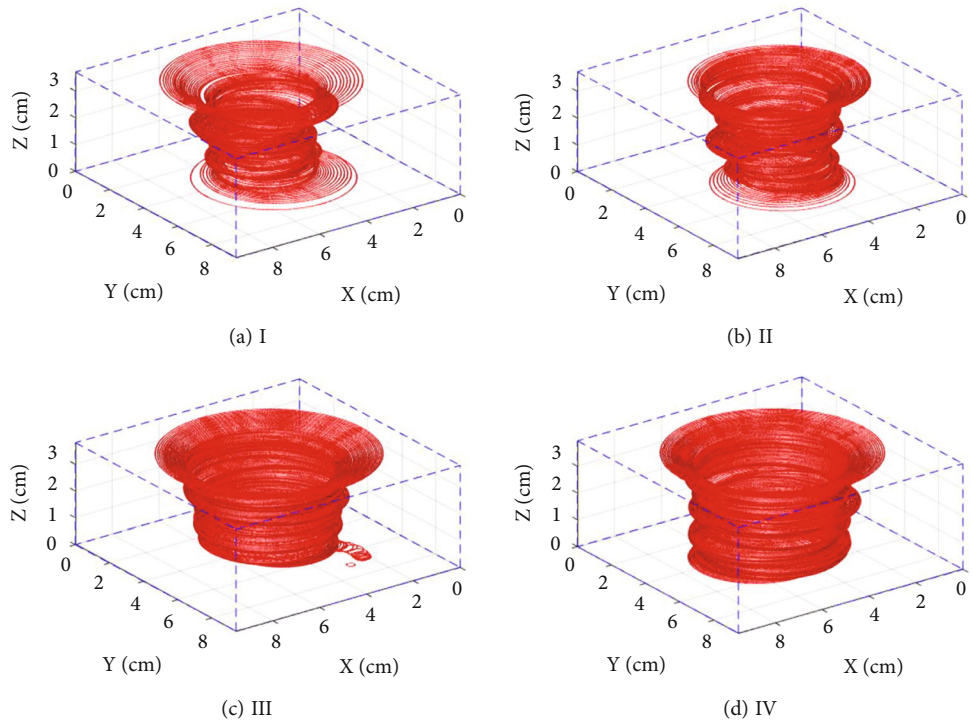

Figure 9: Equivalent drainage channel.

perimeter of void, and P_c is the perimeter of a circle equal to the area of the void.

Figure 8 shows the distribution of perimeter variation coefficient in samples I~IV.

It can be seen that the values less than 1.06 account for 93.98%, 92.5%, 88.00%, and 85.01%, respectively, in samples I~V; likewise, the values larger than 1.06 account for 6.07%, 7.50%, 12.00%, and 14.99%, respectively. It can be concluded that the perimeter variation coefficient of samples with more void content is generally larger than that with less void content. The larger perimeter variation coefficient means that the perimeter contacting with the water flow becomes larger, which produces greater resistance to the water flow and is not conducive to the pavement drainage.

It is easy to imagine that larger area for water passing on a cross section will show greater drainage capacity. Considering the interconnected pores as a whole pipe with only one water passing channel, take the centroid of all the voids on each CT images as the center of the pipe, and take the accumulated area value of each void on an image as the area of the channel; then, draw a circle on each cross section, respectively, as shown in Figure 9. It can be seen that the size of the channel near the top is larger than that near the middle and lower part. The size of channels with larger sample number is generally larger than that with smaller sample number, indicating that sample with larger void content tends to show better drainage performance.

7. Further Research

Although the 3D geometry of pore structures in PA concrete has been successfully reconstructed, it still remains a challenge to propose several key parameters for describing the geometry characteristics. Besides, there is no doubt that the drainage performance of pavement is related to the shape, size, roughness, and other related parameters of interconnected pores, but there is still a lack of effective way to obtain these parameters to evaluate its drainage performance, which needs further research.

8. Conclusions

This paper is aimed at researching the relationship between 3D pore structures and drainage performance of PA concrete. Four samples were formed and scanned by CT equipment to obtain the internal cross-sectional CT images. Image processing technology and OTSU method were conducted to deal with these CT images for segmenting them into three subimages (void image, asphalt mortar image, and aggregate image) according to the three components of PA concrete. The voids on void images were identified and classified into three groups according to the three kind of pores (interconnected pore, semi-interconnected pore, and closed pore) and reshaped them into 3D pore structures. Then, the volume and size distribution of the pores was analyzed. Besides, this research mainly focused on the influence of several parameters obtained from interconnected pores on the drainage performance of PA concrete at last. The conclusions are as follows:

(1) Image dodging plays an important role in CT image segmentation process. 2D gamma dodging shows an excellent performance in unifying the illumination component of CT images to improve the image segmentation effect

(2) Pore structures in PA concrete can be classified into three types according to the interconnectivity, including interconnected pore, semi-interconnected pore, and closed pore. Pore structures in the PA concrete can be reconstructed according to the overlapping principle

(3) PA concrete generally contains a lot of pores, most of which are closed pores, but their cumulative volume only accounts for about 0.5% of the total pore volume. The other small parts are semi-interconnected pores and interconnected pores; however, their cumulative volume accounts for more than 99% of the total pore volume

(4) The void size is mainly distributed below 2.61 mm, most of which belongs to interconnected pores. The size of voids belonging to closed pores and semi-interconnected pores is mainly distributed below 5.21 mm. With the increase of void content, the proportion of void with large size gradually increases

(5) There is a highly linear positive correlation between permeability coefficient and void content. The correlation coefficient reaches 0.998. The permeability coefficient also shows a high linear correlation with the measured void content, and the correlation coefficient reaches 0.987

(6) Hydraulic radius is mainly distributed below 0.88 mm. With the increase of void content, the number of larger voids increases gradually, indicating that the drainage capacity increases in a sense. The geometry of pore structures in PA concrete is extremely complex. Meanwhile, almost all the values of A_1/A_2 are less than 1, indicating that the size of voids near the top is larger than that near the bottom

(7) The perimeter variation coefficient of samples with more void content is generally larger than that with less void content. The larger perimeter variation coefficient means that the perimeter contacting with the water flow becomes larger, which produces greater resistance to the water flow and is not conducive to the pavement drainage. PA concrete with larger void content is more likely containing larger water passing channel, which tends to show a better drainage performance

Data Availability

Some or all data that support the findings of this study are available from the corresponding author (xiejg@nuaa.edu.cn) and first author (wangzq911201@nuaa.edu.cn) upon reasonable request.

Conflicts of Interest

The authors declare that they have no known competing financial interests or personal relationships that could have appeared to influence the work reported in this paper.

Acknowledgments

This study was supported by the National Key R&D Program of China (2018YFB1600101), National Natural Science Foundation of China (51908286), and Natural Science Foundation of Jiangsu Province (BK20191278). Also, all the authors of the following references are much appreciated.

References

[1] P. P. Guo, F. F. Liu, G. Lei et al., "Predicting response of constructed tunnel to adjacent excavation with dewatering," *Geofluids*, vol. 2021, Article ID 5548817, 17 pages, 2021.

[2] Y. Wang, W. K. Feng, H. J. Wang, C. H. Li, and Z. Q. Hou, "Rock bridge fracturing characteristics in granite induced by freeze-thaw and uniaxial deformation revealed by AE monitoring and post-test CT scanning," *Cold Regions Science and Technology*, vol. 177, article 103115, 2020.

[3] H. N. Wu, P. Li, T. F. Nian, G. H. Zhang, T. He, and X. Y. Wei, "Evaluation of asphalt and asphalt mixtures' water stability method under multiple freeze-thaw cycles," *Construction and Building Materials*, vol. 228, article 117089, 2019.

[4] J. G. Xie, C. H. Wu, H. Li, and G. T. Chen, "Study on stormwater management of grassed swales and permeable pavement based on SWMM," *Water*, vol. 9, no. 11, p. 840, 2017.

[5] Y. Wang, Y. F. Yi, C. H. Li, and J. Q. Han, "Anisotropic fracture and energy characteristics of a Tibet marble exposed to multi-level constant-amplitude (MLCA) cyclic loads: a lab-scale testing," *Engineering Fracture Mechanics*, vol. 244, article 107550, 2021.

[6] M. Z. H. Mahmud, N. A. Hassan, M. R. Hainin et al., "Characterisation of microstructural and sound absorption properties of porous asphalt subjected to progressive clogging," *Construction and Building Materials*, vol. 283, article 122654, 2021.

[7] P. Rungruangvirojn and K. Kanitpong, "Measurement of visibility loss due to splash and spray: porous, SMA and conventional asphalt pavements," *International Journal of Pavement Engineering*, vol. 11, no. 6, pp. 499–510, 2010.

[8] X. Ma, J. W. Jiang, Y. J. Zhao, and H. Wang, "Characterization of the interconnected pore and its relationship to the directional permeability of porous asphalt mixture," *Construction Building Materials*, vol. 258, article 121233, 2020.

[9] M. Z. H. Mahmud, N. A. Hassan, M. R. Hainin, and C. R. Ismail, "Microstructural investigation on air void properties of porous asphalt using virtual cut section," *Construction and Building Materials*, vol. 155, pp. 485–494, 2017.

[10] W. L. Wu, D. Y. Wang, X. N. Zhang, and Z. Li, "Air voids distribution of asphalt mixtures based on industrial computerized tomography," *Journal of Central South University*, vol. 43, no. 6, pp. 2343–2348, 2012.

[11] F. Zhang, R. S. Chen, and F. J. Ni, "Techniques of permeability testing for porous asphalt pavement mixture," *Journal of Southeast University*, vol. 40, no. 6, pp. 1288–1292, 2010.

[12] W. Jiang, A. Sha, and J. Xiao, "Experimental study on relationships among composition, microscopic void features, and performance of porous asphalt concrete," *Journal of Materials in Civil Engineering*, vol. 27, no. 11, article 04015028, 2015.

[13] N. A. Hassan, M. Z. H. Mahmud, K. A. Ahmad, M. R. Hainin, R. P. Jaya, and N. Mashros, "Air voids characterisation and permeability of porous asphalt gradations used in different

countries," *Journal of Engineering and Applied Science*, vol. 11, pp. 14043–14047, 2016.

[14] A. Garcia, M. Aboufoul, F. Asamoah, and D. Jing, "Study the influence of the air void topology on porous asphalt clogging," *Construction and Building Materials*, vol. 227, article 116791, 2019.

[15] I. Gruber, I. Zinovik, L. Holzer, A. Flisch, and L. D. Poulikakos, "A computational study of the effect of structural anisotropy of porous asphalt on hydraulic conductivity," *Construction and Building Materials*, vol. 36, pp. 66–77, 2012.

[16] Y. J. Zhao, X. W. Wang, J. W. Jiang, and L. Zhou, "Characterization of interconnectivity, size distribution and uniformity of air voids in porous asphalt concrete using X-ray CT scanning images," *Construction and Building Materials*, vol. 213, pp. 182–193, 2019.

[17] Y. Wang, C. H. Li, and J. Q. Han, "On the effect of stress amplitude on fracture and energy evolution of pre- flawed granite under uniaxial increasing-amplitude fatigue loads," *Engineering Fracture Mechanics*, vol. 240, article 107366, 2020.

[18] E. S. H. Garcia, L. P. Thives, E. Ghisi, and L. N. Antunes, "Analysis of permeability reduction in drainage asphalt mixtures due to decrease in void volume," *Journal of Cleaner Production*, vol. 248, article 119292, 2020.

[19] M. Aboufoul, A. Chiarelli, I. Triguero, and A. Garcia, "Virtual porous materials to predict the air void topology and hydraulic conductivity of asphalt roads," *Powder Technology*, vol. 352, pp. 294–304, 2019.

[20] T. F. Fwa, E. Lim, and K. H. Tan, "Comparison of permeability and clogging characteristics of porous asphalt and pervious concrete pavement materials," *Transportation Research Record Journal of the Transportation Research Board*, vol. 2511, no. 1, pp. 72–80, 2015.

[21] Z. Q. Wang, J. G. Xie, L. Gao, Y. P. Liu, and L. Tang, "Three-dimensional characterization of air voids in porous asphalt concrete," *Construction and Building Materials*, vol. 272, article 121633, 2021.

[22] S. Li, H. Wang, L. Y. Wang, X. Z. Yu, and L. Yang, "Adaptive dodging method based on variational mask for remote sensing images," *Journal of Remote Sensing*, vol. 22, no. 3, pp. 450–457, 2018.

[23] R. Pullagura, U. S. Valasani, and P. P. Kesari, "Hybrid wavelet-based aerial image enhancement using georectification and homomorphic filtering," *Arabian Journal of Geosciences*, vol. 14, no. 13, p. 1235, 2021.

[24] W. D. Liu, J. Y. Li, W. B. Zhang, and L. Li, "Underwater image enhancement method with non-uniform illumination based on Retinex and ADMM," *Journal of Northwestern Polytechnical University*, vol. 39, no. 4, pp. 824–830, 2021.

[25] C. Wang, X. J. Xue, H. Li, G. Y. Zhang, H. R. Wang, and L. Zhao, "Underwater image enhancement based on color correction and improved 2D gamma function," *Journal of Electronic Measurement and Instrumentation*, vol. 35, no. 2, pp. 171–178, 2021.

[26] G. X. Li, B. Y. Zhang, and Y. Z. Yu, *Soil Mechanics*, Tsinghua University Press, 2nd edition, 2013.

[27] Y. L. Wang, *Hydromechanics*, China Communications Press Co. Ltd., 2nd edition, 2015.

[28] P. P. Guo, X. N. Gong, Y. X. Wang, H. Lin, and Y. Zhao, "Minimum cover depth estimation for underwater shield tunnels," *Tunnelling and Underground Space Technology*, vol. 115, article 104027, 2021.